Using ghost fronts within STEREO Heliospheric Imager data to infer the evolution in longitudinal structure of a coronal mass ejection

Article

Accepted Version

To link to this article DOI: http://dx.doi.org/10.1029/2018SW002093

Publisher: American Geophysical Union

Using Ghost fronts within STEREO Heliospheric Imager data to infer the evolution in longitudinal structure of a Coronal Mass Ejection

C. J. Scott[1*], M. J. Owens[1†], C. A. de Koning[2,3‡], L. A. Barnard[1§], S. R. Jones[1¶], J. Wilkinson[4]

‖

[1]Department of Meteorology, University of Reading, Berkshire, UK, RG6 6BB
[2]Cooperative Institute for Research in Environmental Sciences, University of Colorado, Boulder, CO 80309, USA
[3]NOAA Space Weather Prediction Center, Boulder, CO 80305, USA
[4]Zooniverse c/o Department of Astrophysics, University of Oxford, UK

Key Points:

- Multiple fronts observed in STEREO Heliospheric Imager data can be used to infer the longitudinal structure of a CME
- Simple geometric models do not represent the physical evolution of a CME expanding into a structured background solar wind

*https://orcid.org/0000-0001-6411-5649
†https://orcid.org/0000-0003-2061-2453
‡https://orcid.org/0000-0002-9577-1400
§https://orcid.org/0000-0001-9876-4612
¶https://orcid.org/0000-0002-7716-3532
‖https://orcid.org/0000-0001-8505-4494

Corresponding author: C. J. Scott, chris.scott@reading.ac.uk

Abstract

Images of coronal mass ejections (CMEs) from the Heliospheric Imager (HI) instruments on board the STEREO spacecraft frequently contain rich structure. Here, we present analysis of the Earth-directed CME launched on 12 December 2008 in which we intepret the revealed structure as projections of separate discrete sections of the physical boundary of the CME. By comparing the relative position of the outer and inner 'ghost' fronts seen in the STEREO HI1 cameras with the positions of features determined from three CME models we show that the two fronts seen in the images correspond to the expected position of the flank and nose of the CME where the background solar wind is uniform. In contrast, the flank of the CME observed expanding into a structured background solar wind results in the elongation between the two fronts being greater than expected. This is consistent with the CME flank distorting in the presence of a high-speed solar wind stream. Further work is required to consolidate these results. The presence of a shock for this event was ruled out by consideration of the low CME speed and by studying in-situ spacecraft data. The CME flank crossing the Thomson sphere was also ruled out as a cause of the ghost fronts. Ghost fronts could provide information about the longitudinal shape of the CME independent of geometric models. This technique could subsequently be used to improve space weather forecast models through techniques such as data assimilation.

1 Introduction

The Heliospheric Imagers (Eyles et al., 2009) on board the twin STEREO spacecraft (Kaiser, 2005) have returned remarkable images of interplanetary CMEs revealing detailed and often intricate structures within each eruption. During the first four years of the mission, the spacecraft were in a geometry that enabled the HI instruments to image Earth-directed transients from outside the Sun-Earth line. In principle, this view point enables the radial speed of CMEs to be estimated directly from the images rather than inferred from the expansion rate of a CME as viewed along the Sun-Earth line. Techniques developed for estimating the speed, v, and direction of transients relative to the observer, ϕ (N. R. Sheeley et al., 1999) were extended to the HIs (N. R. Sheeley Jr. & Rouillard, 2010; Rouillard et al., 2011). These 'fixed phi' techniques use the assumption that a CME is traveling at a constant speed and use the apparent acceleration within a sequence of images to infer a constant direction of CME propagation relative to the observer. This technique, which treats the transient as a single-point, was soon extended to account for the three-dimensional geometry of a CME. The Harmonic Mean method (Lugaz, Vourlidas, & Roussev, 2009) treats a CME as an expanding sphere with one limb anchored to the Sun (known as the Harmonic Mean fitting technique), while the Self-Similar-Expansion technique (Davies et al., 2012) assumes a spherical CME whose radius changes as it expands from the Sun in such a way that it has a constant angular width. The Harmonic Mean and fixed-phi models are examples of the self-similar expansion model with the half width of the CME set to 90^o and 0^o respectively. In all these techniques, the apparent elongation angle of the CME from the Sun is estimated by taking slices through the HI images (most often along the ecliptic) and stacking these to form a 'J-map' - a plot of image brightness as a function of elongation and time. On a J-map, a transient appears as a bright feature with a positive gradient. These features are then (usually manually) scaled and a two parameter fit in speed and direction is carried out. All these techniques make assumptions about the extent of a three-dimensional structure from two-dimensional images. Recent work (Barnard et al., 2017) on a subset of Earth-directed CMEs, for which arrival times at Earth were available from in-situ observations at the L1 point, took initial values of CME speed, angular extent and propagation direction from coronagraph data and, using these, investigated the efficacy of these geometrical models in predicting the speed and time of a CME's arrival at Earth. Their work showed that, despite minimizing the uncertainties in all known variables, none of these techniques were able to generate physically realistic and consistent predictions from both spacecraft within the expected uncertainties. They concluded that the assumptions about a symmetric CME geometry did not adequately describe the evolution of a CME. This is unsurprising. An interplanetary CME should not be considered as a coherent structure since the longitudinal expansion rate of a CME quickly exceeds the Alfvén speed of the solar wind plasma, preventing information to be transmitted across a CME front (Owens et al., 2017). A more realistic physically constrained model of CME evolution (Owens et al., 2006) follows an initially circular flux rope CME as it becomes distorted in a constant solar wind flow. This Kinematically Distorting Flux Rope (KDFR) model was subsequently extended to consider CME distortions generated by a CME expanding into a non-uniform solar wind (Owens, 2006).

2 Multiple Fronts in HI images

One characteristic that seems to be extremely common among CMEs observed by the HI-1 cameras is the presence of a secondary 'ghost' front that is similar in shape to the observed outer edge of the event but separated by a few degrees in elongation. The intensities seen in each pixel of an HI image result from Thomson scattering of sunlight by electrons integrated along the line of sight. A bright feature within an image can therefore be interpreted as a discrete, relatively dense region of solar wind plasma, contributions from an extended region of plasma distributed along the line of sight, or a combination of the two. In any given line of sight, the weight given to a particular solar wind structure depends on its density and its distance from the Thomson Sphere. In a spherically symmetrical solar wind plasma whose density decreases with distance from the Sun, this will correspond to the point closest to the Sun. For an observer at a distance from the Sun, this region of enhanced weighting describes a sphere whose diameter lies between the observer and the Sun - known as the Thomson Sphere. It is conceivable therefore that multiple enhanced returns may result from the same extended feature, both where the plasma density is enhanced at the front of the CME and where that structure crosses the Thomson sphere. Modelling work by Manchester IV et al. (2008) demonstrated such behaviour for a CME in synthetic HI-2 images. The Thomson Sphere is better called the Thomson Plateau, a broad region centered on the Thomson Sphere that is about $50-60^o$ wide, where the scattered white light has approximately equal intensity (Howard, 2011; Howard & DeForest, 2012). Alternatively, multiple fronts may result from the same extended feature corresponding to both the dense region of plasma accumulating at the leading edge, or 'nose', of a CME and the extended region of plasma along the flank of the CME corresponding to the tangent of the structure with respect to the observer (figure 1). Some authors have interpreted the multiple fronts as a pile up of material corresponding to the position of a shock ahead of the material being swept up by the magnetic cloud within the CME (Pant et al., 2016). Lugaz et al. (2012) discuss the complexity of confidently associating features in HI images with different components of CME structure.

3 The CME of 12 December 2008

STEREO was launched into one of the deepest solar minima for a century (see, for example, the sunspot data at `http://sidc.be/silso/`) and so there were few Earth-directed events occurring during the early phase of the mission, with the spacecraft separated from the Earth by an Earth-Sun-Spacecraft angle of 42 degrees. We note that this is similar to potential new operational space weather missions situated near the L5 point.

In the current paper, we consider the multiple 'ghost' fronts observed in HI images during the CME of 12 December 2008. This was the first Earth-directed CME to be tracked to Earth with the HI instruments on board both STEREO spacecraft and so has been

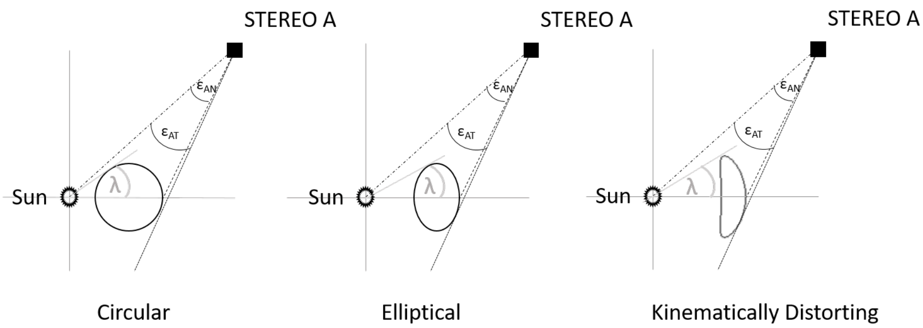

Figure 1. Three cartoons demonstrating the difference in elongation angle for the nose (ε_{AN}) and tangent point (ε_{AT}) of a circular (left), elliptical (center) and Kinematically Distorted (right) CME. In each case, the CME is assumed to expand with a constant longitudinal half-width, λ

the subject of much analysis (Davis et al., 2009; Liu et al., 2010; Byrne et al., 2010). Davis et al. (2009) tracked three features observed in images from the HI instruments on both spacecraft. Adopting the techniques developed by N. R. Sheeley et al. (1999) and N. R. Sheeley Jr. and Rouillard (2010), they tracked these features in time/height profiles (J-maps) independently for each spacecraft and showed that the arrival time of the first feature at Earth was consistent with a constant propagation speed of 411 ± 23 kms^{-1} for HI-A and 417 ± 15 kms^{-1} for HI-B. Subsequently Liu et al. (2010) used J-maps to identify transient features in both STEREO spacecraft and, assuming that both spacecraft were observing the same isolated feature, triangulated on this point to determine the location and movement of that feature in the equatorial plane. A CME is a three-dimensional structure and, as the authors themselves state; *However, the imaging observations provide integrated line-of-sight information through a three-dimensional structure. Projection and Thomson-scattering effects may affect the tracks in the time-elongation maps in ways that are difficult to assess quantitatively without detailed modelling of the coronal brightness.* Barnard et al. (2017) discuss the limitations in feature tracking using J-maps rather than through tracking fronts in the images. A comparison of predicted arrival of the fronts at 1 AU presented by Liu et al. (2010) is consistent with the in-situ data at L1. However, the extended region of enhanced solar wind density seen ahead of the CME allows for considerable uncertainty in the predicted arrival time of the first front and the second front coincides with an enhancement that is barely greater than ambient solar wind. It should be noted that Davis et al. (2009) achieved similar, if not better, agreement with the in-situ data from their analysis by tracking an entirely different third front seen in the HI images.

One consequence of assuming a line-of-sight integration of scattered light is coming from a point source (as is done in the analysis of Liu et al. (2010)) is that any asymmetric expansion of an extended 3-D structure will manifest itself as a change in propagation direction, as was presented their analysis. Here we use an empirical model (described by Riley, Linker, and Miki (2001) and available at `http://www.predsci.com/mhdweb/home.php`) to examine the background solar wind for the epoch of this event (figure 2). This model suggests that while the background solar wind encompassing the nose and eastward flank of the CME (as observed from HI-A) was indeed uniform and relatively slow, the westward portion of the CME was expanding into a stream of fast solar wind and so would be expected to evolve asymmetrically compared with the eastern flank.

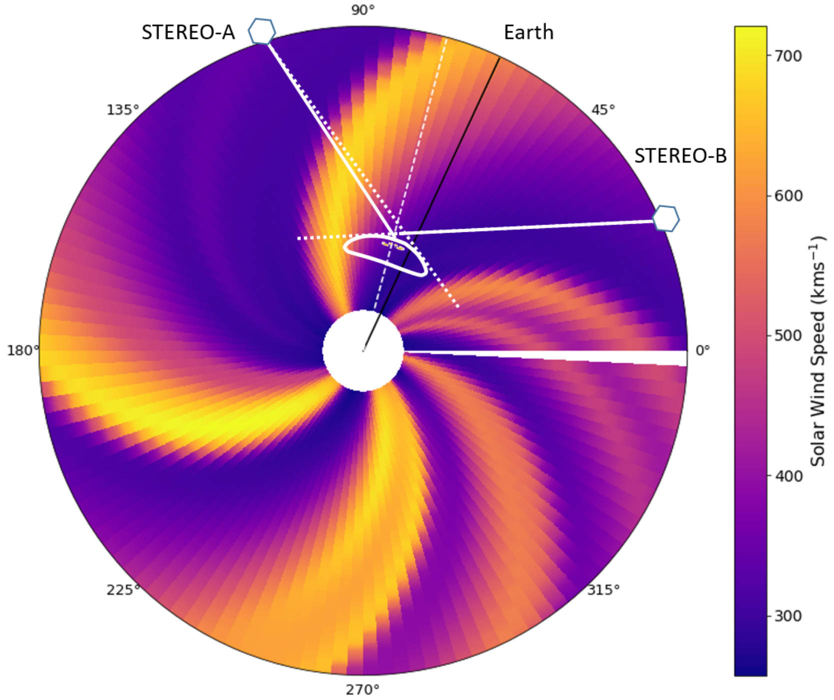

Figure 2. The CME of 12 December 2008 (here represented in white as a kinematically distorting flux rope) overlaid on the modeled background solar wind field. The nose and eastern flank of the CME (as observed from STEREO-A) is expanding into a uniform region of slow solar wind. In contrast, the western flank of the CME (as observed from STEREO-B) is expanding into a region which includes a fast solar wind stream. Lines of sight from the spacecraft to the CME nose are represented as a white solid line while lines of sight from the spacecraft to the CME flanks (tangent to the front) are represented as dotted lines. The CME direction of propagation (as determined from coronagraph observations) is represented by a white dashed line and the Sun-Earth line is represented by a solid black line.

Lugaz et al. (2010) considered a set of four CMEs, including the event of 12 December 2008, and made estimates of their azimuthal properties by the application of a pair of models that assumed either a spherical CME connected to the Sun expanding into the heliosphere with a varying direction of propagation or a spherical CME expanding along a fixed direction with a variable radius. For the 12 December 2008 CME, they found the two brightest features to be propagating along longitudes separated by around 10^o. Both these models assume a symmetrically expanding front. Any asymmetry in the expansion of the actual CME (as would be expected in the case of the 12 December 2008 CME) could explain this apparent difference in propagation direction.

All of the analyses described above are valid attempts to model this CME given the current information available. Assumptions need to be made in order to fill in the gaps necessary to estimate the size, shape, speed and propagation direction of a CME. We here present an alternative approach, in which the initial shape and position of the CME is characterized from coronagraph data. An assumption is then made that its half width remains constant as it propagates and the two fronts observed in the HI images from a single spacecraft (figure 4) are interpreted as two sections of the same front. In this way, no assumption is made about the evolution of the CME shape other than of it expanding with a constant angular width. Instead, the relative separation of these fronts can be used to infer information about the longitudinal properties of the CME. By comparison with established CME propagation models, we show that our results are broadly consistent with geometric models where the background solar wind is constant but deviates from these where the background solar wind is more structured. Nevertheless the observations are consistent with the expected distortion of the CME front. Since we are determining the CME half-width from coronagraph data, we here do not consider the Harmonic Mean technique as this effectively assumes a CME half-width of 90^o.

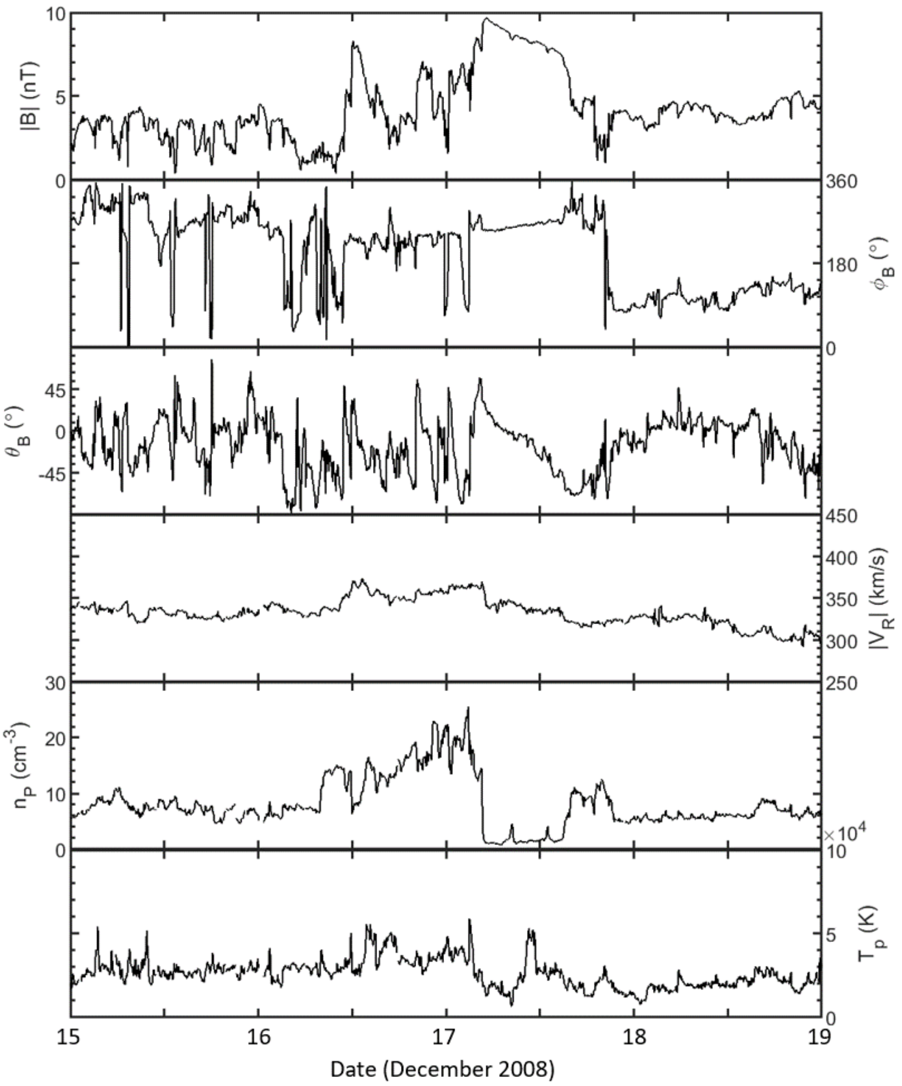

Figure 3. In-situ solar wind data at L1 as measured by the ACE spacecraft. From top to bottom panels the parameters are; total magnetic field, magnetic field azimuth angle, magnetic field inclination angle, radial speed, proton concentration and temperature.

While there is some range in predicted values for the speed and direction of this event, all studies conclude that this event was Earth-directed, with an average radial speed between the Sun and the Earth of approximately $400 kms^{-1}$. Such a speed is usually insufficient to generate a shock ahead of the CME, although Owens, Cargill, Pagel, Siscoe, and Crooker (2008) and Lugaz et al. (2017) demonstrated that this can sometimes happen. Slow CMEs can still drive shocks but they do so by either expanding (so while the average speed is low, the leading edge speed can be relatively high) or by propagating into very slow upstream wind ($300 kms^{-1}$ or less). For the December 2008 ICME, neither is really applicable (figure 3). The in-situ data, recorded by the ACE spacecraft (Stone et al., 1998) as the transient swept past the L1 point upstream of the Earth contains little evidence of continued expansion and the upstream solar wind is approximately $340 kms^{-1}$. There is some compression of the upstream solar wind but there is no obvious shock at 1 AU. While the CME may have been initially traveling faster than this average speed, it is unlikely, in this instance, that a shock traveling ahead of the CME magnetic cloud can explain the multiple fronts observed in HI data.

4 Analysis of coronagraph data

Multiple, independent methods were used to reconstruct the CME in the coronagraph field of view. One of the methods is an extension of SWPC-CAT (Millward et al., 2013), which is a tool that uses a 3D, balloon-like shape to visually match the white-light image observed by STEREO-A, STEREO-B, and SOHO corresponding to the outer, dense leading edge of the CME. The fitting tool we used differs from SWPC-CAT, in that the shape used to approximate the CME can have an elliptical cross-section; in addition, the curvature of the leading edge can be changed from a flat leading edge (a cone with no ice cream) to a highly rounded leading edge (a cone with a generous scoop of ice cream). Another method we used is a purely geometric technique, geometric localization (Pizzo and Biesecker (2004); de Koning, Pizzo, and Biesecker (2009)). The third method we used is the method of equal masses (Colaninno & Vourlidas, 2009).

The angular extent of the CME was determined using enhanced SWPC-CAT, only. The East-West half-width was estimated to be 21 ± 3^o while the North-South half-width was estimated to be 23 ± 2^o. So, initially, this CME had a nearly circular cross-section. The initial position of the CME leading edge within the coronagraph data was estimated to be at a radial distance of 7.9 ± 0.4 solar radii at 10:37 on 12 December 2008.

The latitude of propagation was estimated using two of the above methods. Using enhanced SWPC-CAT with two or three spacecraft, resulted in a latitude of 8 ± 1^o in Heliocentric Earth Equatorial (HEEQ) coordinates, slightly north of the solar equator. The estimated latitude did not strongly depend on whether two or three spacecraft were used, or on the curvature of the leading edge. Using the purely geometric technique, the latitude of propagation was found to be similar, 10 ± 3^o HEEQ. The method of equal masses is not sensitive to the latitude of propagation; therefore, that technique is not applicable. Combining these results in an ensemble of (two) methods, results in a latitude of 9 ± 2^o in HEEQ coordinates. The longitude of propagation was estimated using all three methods. Using enhanced SWPC-CAT with two or three spacecraft and balloon shapes with various leading-edge curvature, resulted in a longitude of 10 ± 2^o HEEQ, slightly west of the Sun-Earth line. Using geometric localization, the longitude was estimated to be 8 ± 1^o HEEQ. The method of equal masses generated a value of 17 ± 3^o HEEQ. Combining all analyses in an ensemble of techniques (in which approximately equal weight is given to each method), results in a longitude of 10 ± 4^o in HEEQ coordinates.

The CME speed within the coronagraph field of view was estimated using two different methods. Using enhanced SWPC-CAT, the speed was dependent on the leading-edge curvature. The flatter the leading edge, the lower the speed. For a highly flattened leading-edge, the speed was estimated to be $350 \pm 10 kms^{-1}$; for a rounder cone, the speed was estimated to be $410 \pm 20 kms^{-1}$. Using geometric localization, the speed was estimated to be $390 \pm 40 kms^{-1}$. Combining all results in an ensemble of techniques (in this case, no attempt was made to give equal weight to each shape and method), results in a radial speed of $380 \pm 30 kms^{-1}$.

Analysis of coronagraph data (following the method of Colaninno and Vourlidas (2009)) determined that the CME had a de-projected mass of $2.610^{12} kg$. Epistemic uncertainty due to a lack of knowledge about the CME's morphology and mass distribution (see de Koning (2017)) suggests that the CME's true mass may be 30% higher than the de-projected mass. While Webb and Howard (2012) have carried out a more recent survey of CME masses, our analysis is more directly comparable with Burkepile, Hundhausen, Stanger, St. Cyr, and Seiden (2004) who looked at limb-event CMEs only as observed by the Solar Maximum Mission, in order to eliminate projection effects. They found an average mass for limb CMEs of 4.5 ± 0.5 10^{12}kg . Thus, this CME is lighter than the average limb CME, even accounting for uncertainty.

Combined with low speed, this was not an energetic CME, which may make it susceptible to distortion. The kinetic energy for this event was 2.0 10^{23} joule (2.0 10^{30}erg). However, according to Burkepile et al. (2004), the average kinetic energy for a limb CME was 2.4 10^{2}4 joule (2.4 10^{31}erg), which is an order of magnitude higher than this event. In fact, the CME parameters detailed above best describe the CME in the outer coronagraph field of view, but do poorly in the inner coronagraph field of view, suggesting that the CME underwent some distortion as it propagated through the STEREO/COR2 field of view.

5 Analysis of Heliospheric Imager data

For the purposes of this analysis, images from only the inner HI1 cameras were used. The main reasons for this was that the plasma density within a CME is greater closer to the Sun and so CMEs appear brighter in HI images since the amount of sunlight scattered through Thomson scattering increases with plasma density. Though the ghost fronts are visible in images from which the background F-corona signal has been subtracted (Figure 4 a), running differenced images, in which two consecutive images are aligned and the difference taken, are used for this analysis since this improves the contrast of the features of interest. As a result, static features within the images are removed while any transient features increase the signal in pixels gaining plasma and decrease the signal in pixels in which plasma has been lost. When imaged in monochrome, a transient moving away from the Sun therefore shows as a feature with a bright leading edge followed by a darker trailing edge.

A sequence of images from each HI1 instrument was examined independently by multiple researchers using tools developed by the Zooniverse team, originally for classifying galaxies (Lintott et al., 2008). The leading edge of each of the two most prominent fronts were identified multiple times in each image by marking them with a series of points. These points were then passed through a kernel density analysis similar to that used in previous analyses (Barnard et al., 2017), the output of which gives the location of each front, along with uncertainties (see figure 4d). The data are then further reduced by considering only the front at the elevation angle corresponding to the ecliptic. In this way, the propagation of the two CME fronts can be plotted as a function of elongation angle, ϵ, against time for each spacecraft.

At this stage it becomes possible to estimate the radial speed of the CME in the HI data. We initially focus on data from HI-A since the nose and flank of the CME observed from this spacecraft fit are expected to be expanding into a uniform solar wind. For the given geometry, the second front - the ghost front, most likely corresponds to the

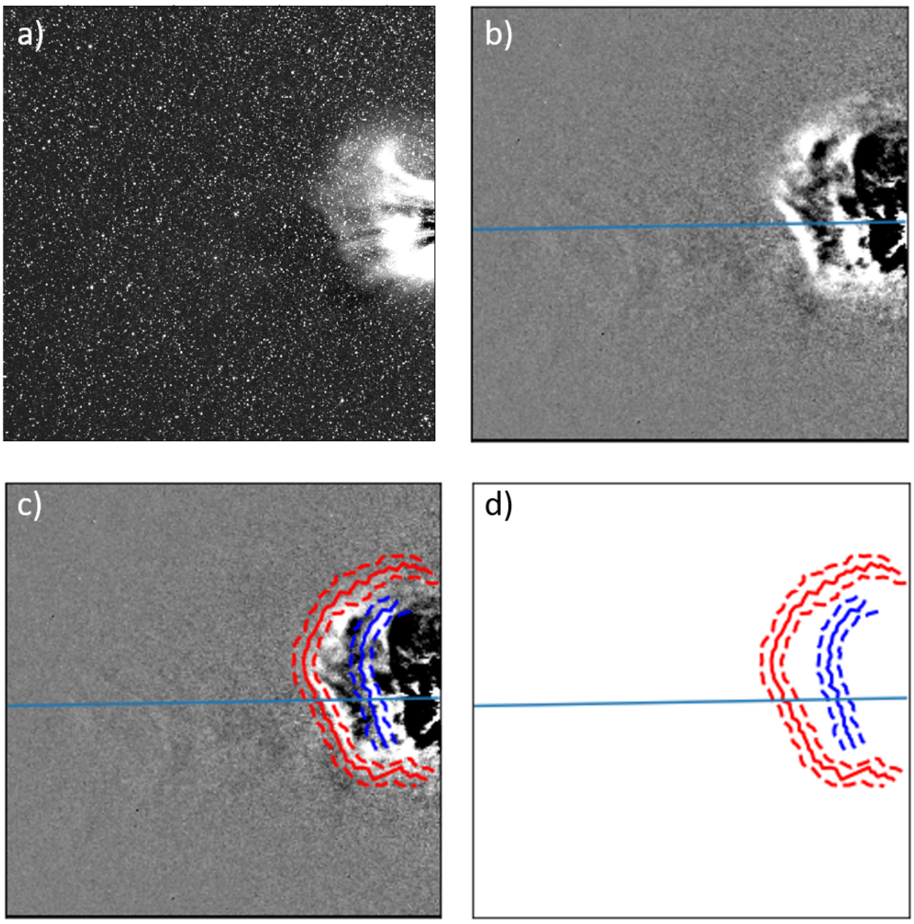

Figure 4. An example HI-A image from 22:49 UT on 12 December 2008 showing a) background subtracted image b) running difference image, c) the same image with the two fronts identified from the kernel density analysis and (d) the fitted fronts alone. We argue that, for this event, the outer and inner fronts correspond to the tangent and nose respectively, of a single CME front. The dotted lines represent the standard error in elongation derived from multiple identifications of each front. The ecliptic is marked with a blue line

leading edge, or nose, of the CME and so this was used to estimate the radial speed. By using the direction of propagation determined from the coronagraph data (10^o west of the Sun-Earth line), the elongations within the HI data can be converted to radial distances. Plotting these as a function of time generated a straight line (Figure 5), indicating that the speed of the CME was constant throughout the HI field of view. A weighted fit to this line gives a speed estimate of $500 \pm 15 km s^{-1}$. It should be noted that this process is analogous to the 'fixed phi' fitting routine for a point source introduced by N. R. Sheeley et al. (1999) and N. R. Sheeley Jr. and Rouillard (2010) although in the current analysis the angle of propagation is determined from the coronagraph data and the subsequent radial speed only calculated after inspection of the resulting distances showed they followed a linear relationship with time. While the radial CME speed measured in HI is greater than the speed estimated from the coronagraph data, it is not inconceivable that the CME underwent further acceleration before reaching radial distances visible within the HI1 field of view. As a sanity check, the CME speed was also estimated from the time taken to propagate from the initial observation within the COR field of view to the first point within the HI field of view that was used in the analysis (34.2±3.3 solar radii at 20:49 on 12 December 2008, assuming a propagation direction of 10^o west of the Sun-Earth line). This was found to be $497 \pm 63 kms^{-1}$, consistent with the radial speed estimated from the HI data alone.

It should be noted that the two fronts identified by Liu et al. (2010), from their scaling of features in the J-map presented in their figure 3, approximate to the outer (tangent) front of our analysis and some other feature that seems to sit at lower elongations than the second front we have identified as the ghost front (see their figure 2). The speed profiles of the features presented in their figure 4 show that they estimated the speed of their outer front to reach speeds in excess of $600 kms^{-1}$, while their inner front reached speeds of around $400 kms^{-1}$. Despite the difference in methods (direction of propagation was a free parameter in their analysis while ours was fixed from the coronagraph observations) it is not unreasonable that the speed we find for our nose front lies between these extremes. Ours is also an average speed derived from HI-1 data only whereas the speeds derived by Liu et al. (2010) correspond to individual times manually scaled from J-maps.

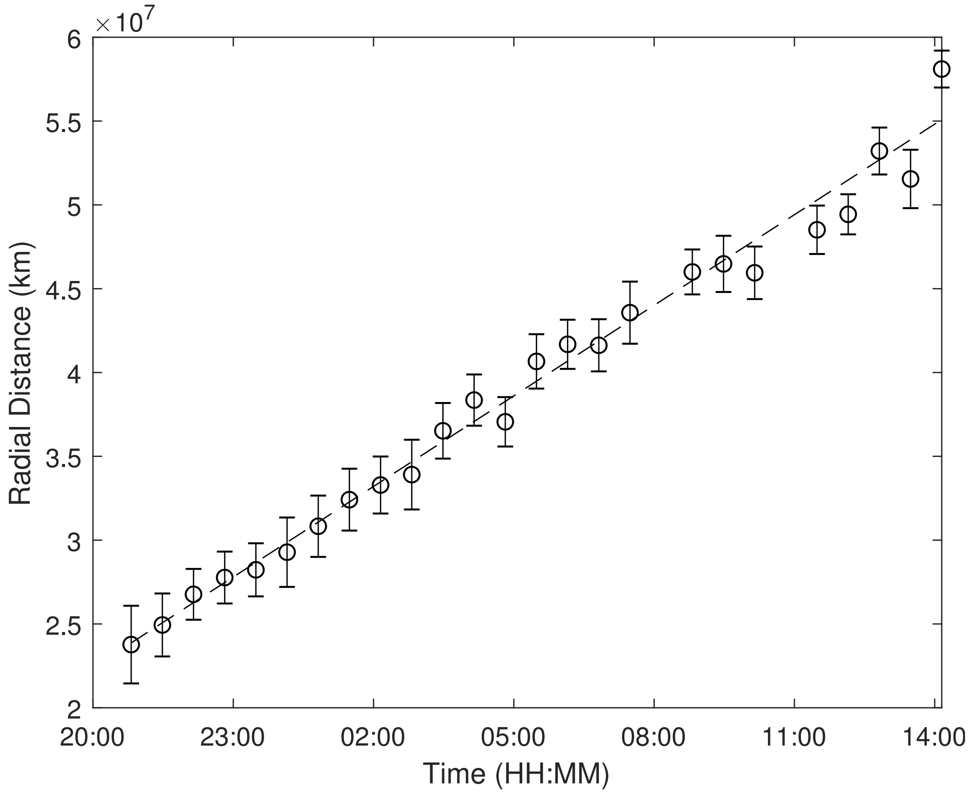

Figure 5. Radial distance versus time for the front corresponding to the leading edge of the CME. Times start on 12 December 2008. Time is in UT. Coronagraph data were used to estimate the direction of propagation (10 degrees west of the Sun Earth line).

In order to model how the nose, tangent point and Thomson sphere crossings would appear in HI images, elongation angles were calculated for the nose (ε_{AN}), tangent (ε_{AT}) and Thomson sphere crossings (ε_{ATS}) in three CME models; Self-Similar Expansion of a circular CME front (SSE-C)(Davies et al., 2012), self-similar expansion of an elliptical CME front (SSE-E)(Rollett et al., 2016) and a Kinematically Distorting Flux Rope

(KDFR)(Owens et al., 2006). These models took their initial conditions (half-width, λ=21, and direction of CME propagation with respect to the observer, $\phi = 32.3^o$) from the analysis of coronagraph data.

The elliptical CME was arbitrarily assumed to have a ratio of 3 : 2 between the major and minor axes. While the elongation angle of the tangent to a circle and ellipse can be derived analytically, for the KDFR model a numerical solution was adopted. For this approach, the nose of the CME was identified, and its elongation (ε_{AN}) calculated geometrically. This angle was then incremented until the resulting spacecraft-CME line did not intercept any points defining the outer boundary of the CME. By adopting this approach, the elongation of the tangent point can be determined to within the increment used (in this case 0.1 degrees). For the KDFR model, a nominal expansion ratio, $A =$ 0.15, was used, as assumed by Owens et al. (2006). The intersections between the CME and the Thomson sphere were also identified, and the elongation of these points (ε_{ATS}) then calculated geometrically. Since the modeled radial speed of the CME sets the gradient of the elongation versus time plot, an initial value of $500kms^{-1}$ was used, as determined from the fit to the HI data. The observer is assumed to be at the location of STEREO-A for the purposes of the initial analysis, since the CME flank expanding into slow, unstructured solar wind will be visible from this viewpoint where the CME expansion is expected to result in the least distortion of the CME front. For this date, the longitudinal separation (STEREO A-Sun-Earth angle) was 42.3^o with the spacecraft at a distance of $0.967AU$. An estimate of the quality of the fit is obtained by calculating R for each front, where R is the root mean square difference between the model and data (in degrees). The KDFR model used assumed that the CME was expanding into a solar wind flowing at a constant speed which, for the flank viewed by STEREO-A, is consistent with the solar wind model for this epoch (figure 2).

6 Results

The results for the three models for HI-A observations are presented in figure 6. In all three models, the outer boundary of the CME does not intercept the Thomson sphere until the CME has propagated sufficiently far into the heliosphere that the resulting elongations (ε_{ATS}) are in excess of 20 degrees. Such intersections cannot account for the multiple fronts seen at much lower elongations in HI-1 images (though they may be apparent at larger elongations in the outer HI2 cameras) and so are discounted as a cause for the ghost fronts. When considering the elongations of the nose (ε_{AN}) and the tangent point (ε_{AT}) in the SSE-C model (that assumes a circular front) (figure 6a), it can be seen that the two modeled fronts are consistently closer in elongation than the two fronts scaled from the HI data. The residual between model and data for the leading edge of this fit, $R_{LE} = 0.092^o$ while the residual between model and data for the tangent front, $R_T =$ 0.168^o. The same two fronts in the SSE-E model (which assumes an elliptical front, figure 6b) diverge in elongation and matched the offset predicted by the model well ($R_{LE} =$ 0.092^o, $R_T = 0.079^o$). While the ratio assumed between the major and minor axes of this elliptical CME is arbitrary, it appears, in this case, to closely model the observations. The results for the KDFR model are presented in figure 6c. Unlike the previous two examples, in this physically constrained model, the CME front evolves in shape as it moves outwards and this too closely models the observations ($R_{LE} = 0.092^o$, $R_T = 0.079^o$).

Having established that the two observed fronts are consistent with enhanced returns from the nose and tangent of a CME propagating into a region of uniform solar wind, and that the SSE-E and KDFR models best represented the shape of the CME in this case, the KDFR model was rerun, allowing the fit parameters to vary within the uncertainties of the observations used to constrain the model.

Since the estimate of radial speed relies on an assumed direction of CME propagation, this calculation was repeated for the range of possible values indicated by the coro-

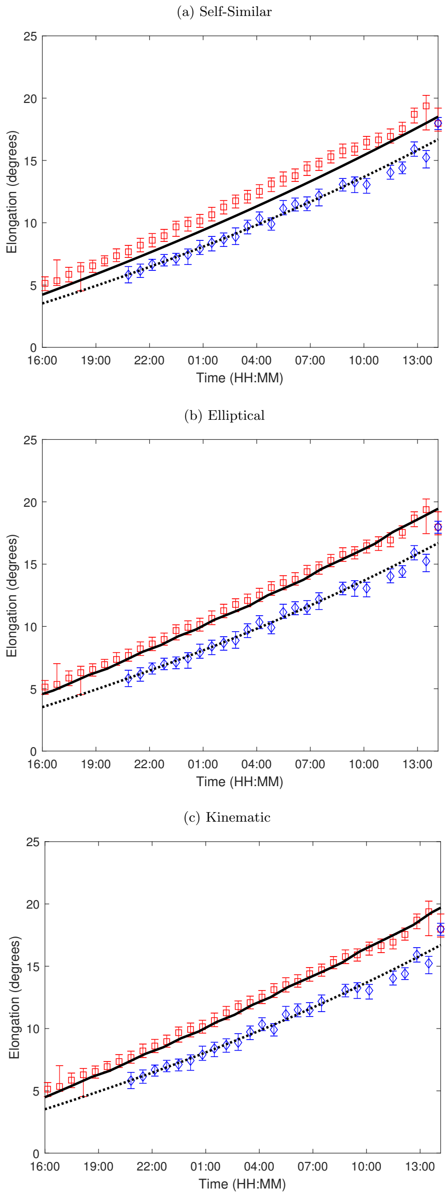

Figure 6. Elongation versus time for modeled elongations of the nose (ε_{AN}, dashed black line) and tangent (ε_{AT}, black solid line) compared with the elongations of the two fronts scaled from STEREO HI1-A data. Times start on 12 December 2008. The results in panel a) assume a circular self-similar expansion model CME, the results in panel b) assume an elliptically expanding CME, while panel c) assumes the front evolves like a Kinematically Distorting Flux Rope. In all cases, the models assume the CME is moving at a radial speed of $500kms^{-1}$. It should be noted that in all the above models, the evolution of the CME nose (dotted line) is the same.

nagraph data. The best fit was achieved for a CME propagating 9^o west of the Sun-Earth line, giving an estimated speed of $496{\pm}15kms^{-1}$. Having ascertained the optimum propagation direction by minimising the residual in fit to the inner front, the optimum half-width of the CME was determined by optimising the fit of the leading front (corresponding to the flank of the CME). This produced a minimum root mean square residual of 0.072^o for $\lambda = 23^o$ (figure 7, left). These values lie within the uncertainties of the coronagraph data from which the initial estimates were made.

That the modeled elongations matched the observations while assuming a CME transit speed of $496{\pm}15kms^{-1}$ between the COR and HI-1 fields of view is further corroboration that the transit speed of the CME was likely higher than that estimated from the coronagraph data alone.

Having established that the ghost fronts conformed to the expected separation and evolution in elongation between the nose and the tangent to a single CME front for conditions in which the CME is propagating into a constant background solar wind, the same analysis was conducted for the HI images taken from STEREO-B assuming the same half-width and propagation direction. As can be seen from figure 2 the direction of travel of the CME is such that from this viewpoint the elongation of the nose (ε_{BN}) and the elongation of the tangent (ε_{BT}) are expected to be more closely aligned than for the view from STEREO-A. The results are presented in figure 7 (right). The fit to CME nose (dotted line, blue data points) in HI-B data is significantly poorer, with an estimated radial speed of $403 \pm 28kms^{-1}$ and a root mean square residual of 0.246^o. This is likely due to the difference between the two instruments with HI-B having a wider point-spread function than HI-A and undergoing greater pointing offsets which reduce the efficiency of background removal in differenced images (Eyles et al., 2009; Tappin, 2017). This makes identifying faint features in HI-B more challenging. Despite these challenges it is apparent that the match to the flank of the CME is poor for the assumed propagation direction and half-width. While the speed fitted to the HI-B data is lower than the estimate obtained from the HI-A data, the two speeds match within two standard errors. Further analysis of the HI-B data revealed that if it were considered independently of the HI-A data, the best fit to the inner front in these images was obtained for a propagation direction of 6^o west of the sun-Earth line, corresponding to a radial speed of $409{\pm}28kms^{-1}$ although the root mean square residual of 0.244^o is not significantly different from the minima obtained when using the parameters determined from the HI-A data. Such a difference could also be interpreted as the plasma build-up at the nose of the CME being extended across a few degrees of solar longitude. It is apparent that the western flank of the CME observed from HI-B is not consistent with a symmetrically expanding front. No realistic value of the CME half-width, λ, can reproduce the observed difference in elongation between these fronts as observed from HI-B while assuming a non-distorted front. Given that the background solar wind is not uniform to the west of the sun-Earth line, we suggest that this flank of the CME would evolve differently from the eastern flank observed by HI-A. This is discussed further in the next section.

7 Discussion and conclusions

The analysis of this event has demonstrated that the ghost fronts seen in HI-A data, for which the CME is expanding into a region of uniform background solar wind, are consistent in elongation with the locations of the CME nose and tangent point. In the geometry of the current example, the second, or 'ghost' front in the HI images appears to correspond to the nose of the CME where a pile-up of plasma ahead of the CME leads to enhanced signal due to Thomson scattering in that region. The speed of the CME outer boundary relative to the ambient solar wind is expected to peak at the leading edge, therefore ambient solar wind compression is expected to peak there too (Siscoe & Odstrcil, 2008; Owens et al., 2008). The outer front seen in the HI images is consistent with the line-of-sight along the tangent of the outer boundary of the CME. While the concentration of solar wind plasma along the extended boundary is likely to be lower than at the CME leading edge, nevertheless there is a sufficient increase in plasma density along this boundary for enhanced signal from Thomson scattering to occur when integrated along the line-of-sight.

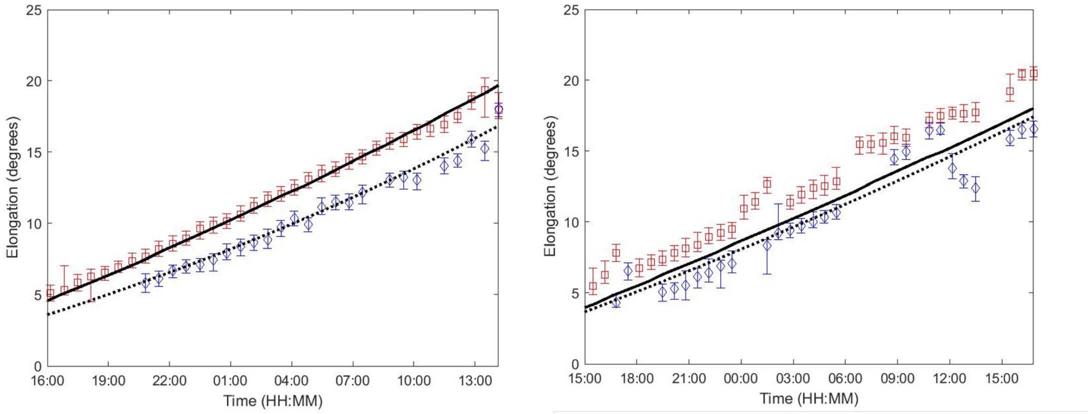

Figure 7. Elongation versus time plot of the same form as figure 6 for HI-A (left) and HI-B(right) both assuming half width, $\lambda = 23^o$ and a direction of 9^o west of the sun-Earth line. These values generated the optimum fit to HI-A data. The assumed propagation direction results in a fitted speed for the nose of the CME of $496 \pm 15 kms{-1}$ in HI-A data and $403 \pm 28 kms{-1}$ in HI-B data. These are consistent within 2 standard errors. Times start on 12 December 2008.

When compared with a range of CME propagation models, for this CME, the best fit to the data came by considering the shape of the CME as an ellipse with a 3:2 ratio between major and minor axes or a kinematically distorting flux rope. The circular self-similar expanding CME front, while broadly reproducing the observations, did not match the data as well as the other two models. It appears therefore that the separation in elongation between the two fronts provides information about the longitudinal shape of the CME front. Both the elliptical and KDFR models require an additional free parameter to be set, (the ratio of major to minor axes and the expansion factor respectively) but since all additional parameters can be estimated from the coronagraph and HI data, this can be iterated to optimize the fit to the observations. The KDFR model has the advantage that it more accurately reproduces the expected distortion of a CME as it propagates in the solar wind and can be extended to account for solar wind structure (Owens, 2006).

The cartoon in figure 2 shows that for a CME with the properties estimated from the coronagraph data, expanding symmetrically into the heliosphere would result in the nose and flank of the CME appearing at similar elongations as viewed from STEREO-B. However, it can be seen that this flank was expanding into a region in which the background solar wind was not uniform. We suggest that presence of a fast solar wind stream at the western flank of the CME has resulted in this portion of the front moving faster, distorting the shape of the CME as indicated by the cartoon shown in figure 8, generating the observed separation in elongation between the nose and flank of the CME, which is larger than expected for a CME expanding into a uniform solar wind.

Current forecasts (Pizzo et al., 2011) characterize a CME in coronagraph data and propagate this using a solar wind model such as Enlil (Odstrcil et al., 2004). It is envisaged that data from the HI cameras could ultimately be used in operational space weather forecasting to refine such a model, either by creating an ensemble of artificial J-maps (as has been demonstrated by Lugaz, Vourlidas, Roussev, and Morgan (2009) and Xiong et al. (2013)) from the model to compare with the data, or through data assimilation of other information gleaned from the HI images.

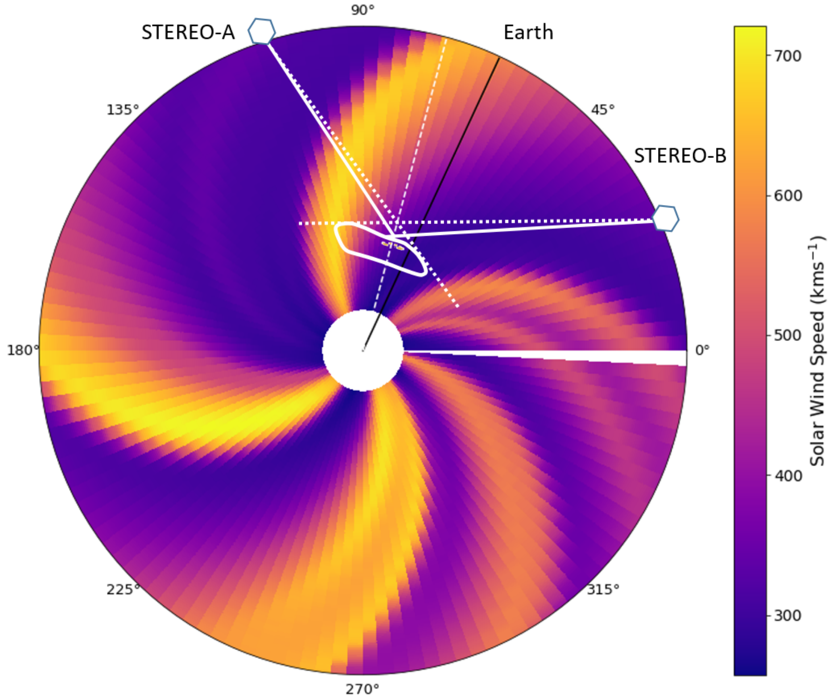

Figure 8. Cartoon illustrating how the presence of a fast solar wind stream on the western flank of the CME could have distorted the CME front, leading to a larger apparent separation in elongation that expected between the CME nose (solid white line) and the flank (dotted whte line) as viewed from the position of the STEREO-B spacecraft.

Information about the longitudinal structure obtained through such analysis of the ghost fronts could potentially be helpful in constraining solar wind forecast models through data assimilation methods to ensure that the shape of the CME front remained consistent with the observations. This is particularly important when tracking an Earth-impacting CME whose direction of propagation is slightly off the Sun-Earth line. In such circumstances, information about the longitudinal shape of a CME will improve estimates of the arrival time and radial speed of the portion of the CME front at Earth.

The separation in elongation of the two fronts is a function of CME width, shape, speed and direction. The elongation at which the two fronts eventually converge occurs when the observer line of sight to the front is perpendicular to the CME propagation direction. For this event, where the CME is propagating around 10^o west of the Sun-Earth line, this occurs at elongation angles of 58^o and 38^o for STEREO-A and STEREO-B respectively. Such elongations lie well outside the HI-1 field of view in this instance. For an Earth-directed CME observed from the L5 Lagrange point this convergence would occur at an elongation angle of 30^o, corresponding to a distance of 0.5 AU.

This study demonstrates that ghost fronts seen in the HI data are consistent with enhanced returns from the nose and tangent of a CME expanding into a uniform solar wind and suggests that solar wind structure can cause deviations from this simple model. It is, nonetheless, a single case study and many more events will need to be analysed in this way before the technique is proven. There is no evidence for a shock in in-situ data for this event and so a shock cannot explain the multiple fronts seen in the HI data. Further work, studying CMEs with a range of speeds and geometries, is needed to determine whether the existence of a shock would complicate the interpretation of multiple fronts seen in HI data. It may also prove valuable to look for ghost fronts in coronagraph data to see whether these too are consistent with enhanced scattering from multiple regions of the same CME front.

To date there have been multiple analyses of the 12 December 2008 CME using a variety of techniques and assumptions to estimate the evolution of this event. Determining which interpretation best represents the CME is a complex question that depends on the criteria by which their individual merits are judged and on the constraints imposed by the available data. Additional analysis considering multiple events will now be carried out to investigate the efficacy of using ghost fronts to infer information on the evolution of CMEs in the inner heliosphere. The KDFR model can be further extended to consider a non-uniform background solar wind (Owens, 2006; Isavnin, 2016) and it will be the subject of further work to see if accounting for the presence of solar wind structure in a time-varying model can reproduce the results presented here.

Acknowledgments

The authors would like to thank the STEREO HI team at the Rutherford Appleton Laboratory and the UK Solar System Data Centre for supplying the Heliospheric Imager data used in this study. The Heliospheric Imager (HI) instrument was developed by a collaboration which included the University of Birmingham and the Rutherford Appleton Laboratory, both in the UK, and the Centre Spatial de Liège (CSL), Belgium, and the US Naval Research Laboratory (NRL), Washington DC, USA. The SECCHI project, led by NRL, involves additional collaborators from LMSAL, GSFC (USA), MPI (Germany), IOTA and IAS (France). Data from the ACE spacecraft The ACE Mission was designed and developed by many organizations and individuals under the support of the Explorer Program in the NASA Office of Space Science. The SOHO/LASCO data used here are produced by a consortium of the Naval Research Laboratory (USA), Max-Planck-Institut fuer Aeronomie (Germany, now Max-Planck-Institut for Sonnensystemforschung), Laboratoire d'Astronomie (France, now Laboratoire d'Astrophysique Marseille), and the University of Birmingham (UK). SOHO is a project of international cooperation between ESA and NASA. Thanks also to Chris Lintott and the Zooniverse team for their continued support. CADK thanks NASA LWS Grant number NNX15AF39G, also known as ProjectZed, for supporting this research. LB and MO thank the UK Science and Technology Facilities Council for support under grants ST/M000885/1 and ST/R000921/1.

Data from the STEREO mission used in this study can be accessed from the UKSSDC at `https://www.ukssdc.ac.uk`. The authors state that they have no conflicts of interest regarding this work.

References

Barnard, L. A., de Koning, C. A., Scott, C. J., Owens, M. J., Wilkinson, J., & Davies, J. A. (2017, June). Testing the current paradigm for space weather prediction with heliospheric imagers. *Space Weather*, *15*, 782-803. doi: 10.1002/2017SW001609

Burkepile, J. T., Hundhausen, A. J., Stanger, A. L., St. Cyr, O. C., & Seiden, J. A. (2004, March). Role of projection effects on solar coronal mass ejection properties: 1. A study of CMEs associated with limb activity. *Journal of Geophysical Research (Space Physics)*, *109*, A03103. doi: 10.1029/2003JA010149

Byrne, J. P., Maloney, S. A., McAteer, R. T. J., Refojo, J. M., & Gallagher, P. T. (2010, September). Propagation of an Earth-directed coronal mass ejection in three dimensions. *Nature Communications*, *1*, 74. doi: 10.1038/ncomms1077

Colaninno, R. C., & Vourlidas, A. (2009, June). First Determination of the True Mass of Coronal Mass Ejections: A Novel Approach to Using the Two STEREO Viewpoints. *The Astrophysical Journal*, *698*, 852-858. doi:

10.1088/0004-637X/698/1/852
Davies, J. A., Harrison, R. A., Perry, C. H., Möstl, C., Lugaz, N., Rollett, T., ... Savani, N. P. (2012, May). A Self-similar Expansion Model for Use in Solar Wind Transient Propagation Studies. *The Astrophysical Journal*, *750*, 23. doi: 10.1088/0004-637X/750/1/23
Davis, C. J., Davies, J. A., Lockwood, M., Rouillard, A. P., Eyles, C. J., & Harrison, R. A. (2009, APR 18). Stereoscopic imaging of an Earth-impacting solar coronal mass ejection: A major milestone for the STEREO mission. *GEOPHYSICAL RESEARCH LETTERS*, *36*. doi: {10.1029/2009GL038021}
de Koning, C. A. (2017, jul). Lessons learned from the three-view determination of CME mass. *The Astrophysical Journal*, *844*(1), 61. Retrieved from https://doi.org/10.3847/1538-4357/aa7a09 doi: 10.3847/1538-4357/aa7a09
de Koning, C. A., Pizzo, V. J., & Biesecker, D. A. (2009, May 01). Geometric localization of cmes in 3d space using stereo beacon data: First results. *Solar Physics*, *256*(1), 167–181. Retrieved from https://doi.org/10.1007/s11207-009-9344-7 doi: 10.1007/s11207-009-9344-7
Eyles, C. J., Harrison, R. A., Davis, C. J., Waltham, N. R., Shaughnessy, B. M., Mapson-Menard, H. C. A., ... Rochus, P. (2009, February). The Heliospheric Imagers Onboard the STEREO Mission. *Solar Physics*, *254*, 387-445. doi: 10.1007/s11207-008-9299-0
Howard, T. A. (2011). Three-dimensional reconstruction of coronal mass ejections using heliospheric imager data. *Journal of Atmospheric and Solar-Terrestrial Physics*, *73*(10), 1242 – 1253. Retrieved from http://www.sciencedirect.com/science/article/pii/S1364682610002427 doi: https://doi.org/10.1016/j.jastp.2010.08.009
Howard, T. A., & DeForest, C. E. (2012). The thomson surface. i. reality and myth. *The Astrophysical Journal*, *752*(2), 130. Retrieved from http://stacks.iop.org/0004-637X/752/i=2/a=130
Isavnin, A. (2016). Fried: A novel three-dimensional model of coronal mass ejections. *The Astrophysical Journal*, *833*(2), 267. Retrieved from http://stacks.iop.org/0004-637X/833/i=2/a=267
Kaiser, M. L. (2005). The STEREO mission: an overview. *Advances in Space Research*, *36*, 1483-1488. doi: 10.1016/j.asr.2004.12.066
Lintott, C. J., Schawinski, K., Slosar, A., Land, K., Bamford, S., Thomas, D., ... Vandenberg, J. (2008, September). Galaxy Zoo: morphologies derived from visual inspection of galaxies from the Sloan Digital Sky Survey. *Monthly Notices of the Royal Astronomical Society*, *389*, 1179-1189. doi: 10.1111/j.1365-2966.2008.13689.x
Liu, Y., Thernisien, A., Luhmann, J. G., Vourlidas, A., Davies, J. A., Lin, R. P., & Bale, S. D. (2010, October). Reconstructing Coronal Mass Ejections with Coordinated Imaging and in Situ Observations: Global Structure, Kinematics, and Implications for Space Weather Forecasting. *The Astrophysical Journal*, *722*, 1762-1777. doi: 10.1088/0004-637X/722/2/1762
Lugaz, N., Farrugia, C. J., Davies, J. A., Möstl, C., Davis, C. J., Roussev, I. I., & Temmer, M. (2012, nov). The deflection of the two interacting coronal mass ejections of 2010 May 23-24 as revealed by combined in situ measurements and heliospehric imaging. *The Astrophysical Journal*, *759*(1), 68. Retrieved from http://stacks.iop.org/0004-637X/759/i=1/a=68?key=crossref.0e7af3d21333a7cad5825389d763f08a doi: 10.1088/0004-637X/759/1/68
Lugaz, N., Farrugia, C. J., Winslow, R. M., Small, C. R., Manion, T., & Savani, N. P. (2017). Importance of cme radial expansion on the ability of slow cmes to drive shocks. *The Astrophysical Journal*, *848*(2), 75. Retrieved from http://stacks.iop.org/0004-637X/848/i=2/a=75
Lugaz, N., Hernandez-Charpak, J. N., Roussev, I. I., Davis, C. J., Vourlidas, A., & Davies, J. A. (2010). Determining the azimuthal properties of coro-

nal mass ejections from multi-spacecraft remote-sensing observations with stereo secchi. *The Astrophysical Journal*, *715*(1), 493. Retrieved from http://stacks.iop.org/0004-637X/715/i=1/a=493

Lugaz, N., Vourlidas, A., & Roussev, I. I. (2009, September). Deriving the radial distances of wide coronal mass ejections from elongation measurements in the heliosphere - application to CME-CME interaction. *Annales Geophysicae*, *27*, 3479-3488. doi: 10.5194/angeo-27-3479-2009

Lugaz, N., Vourlidas, A., Roussev, I. I., & Morgan, H. (2009, May). Solar - Terrestrial Simulation in the STEREO Era: The 24 - 25 January 2007 Eruptions. *Solar Physics*, *256*, 269-284. doi: 10.1007/s11207-009-9339-4

Manchester IV, W. B., Vourlidas, A., Tóth, G., Lugaz, N., Roussev, I. I., Sokolov, I. V., ... Opher, M. (2008, sep). Three-dimensional MHD simulation of the 2003 october 28 coronal mass ejection: Comparison with LASCO coronagraph observations. *The Astrophysical Journal*, *684*(2), 1448–1460. Retrieved from https://doi.org/10.1086/590231 doi: 10.1086/590231

Millward, G., Biesecker, D., Pizzo, V., & de Koning, C. A. (2013). An operational software tool for the analysis of coronagraph images: Determining cme parameters for input into the wsa-enlil heliospheric model. *Space Weather*, *11*(2), 57-68. Retrieved from https://agupubs.onlinelibrary.wiley.com/doi/abs/10.1002/swe.20024 doi: 10.1002/swe.20024

Odstrcil, D., Pizzo, V. J., Linker, J. A., Riley, P., Lionello, R., & Mikic, Z. (2004, October). Initial coupling of coronal and heliospheric numerical magnetohydrodynamic codes. *Journal of Atmospheric and Solar-Terrestrial Physics*, *66*, 1311-1320. doi: 10.1016/j.jastp.2004.04.007

Owens, M. J. (2006, December). Magnetic cloud distortion resulting from propagation through a structured solar wind: Models and observations. *Journal of Geophysical Research (Space Physics)*, *111*(A10), A12109. doi: 10.1029/2006JA011903

Owens, M. J., Cargill, P. J., Pagel, C., Siscoe, G. L., & Crooker, N. U. (2008). Characteristic magnetic field and speed properties of interplanetary coronal mass ejections and their sheath regions. *Journal of Geophysical Research: Space Physics*, *110*(A1). Retrieved from https://agupubs.onlinelibrary.wiley.com/doi/abs/10.1029/2004JA010814 doi: 10.1029/2004JA010814

Owens, M. J., Lockwood, M., & Barnard, L. A. (2017, June). Coronal mass ejections are not coherent magnetohydrodynamic structures. *Scientific Reports*, *7*(1). Retrieved from http://centaur.reading.ac.uk/70996/ doi: 10.1038/s41598-017-04546-3

Owens, M. J., Merkin, V. G., & Riley, P. (2006, March). A kinematically distorted flux rope model for magnetic clouds. *Journal of Geophysical Research (Space Physics)*, *111*, A03104. doi: 10.1029/2005JA011460

Pant, V., Willems, S., Rodriguez, L., Mierla, M., Banerjee, D., & Davies, J. A. (2016). Automated Detection of Coronal Mass Ejections in Stereo Heliospheric Imager Data. *The Astrophysical Journal*, *833*(1), 1–15. Retrieved from http://dx.doi.org/10.3847/1538-4357/833/1/80 doi: 10.3847/1538-4357/833/1/80

Pizzo, V. J., & Biesecker, D. A. (2004, November). Geometric localization of STEREO CMEs. *Geophysical Research Letters*, *31*, L21802. doi: 10.1029/2004GL021141

Pizzo, V. J., Millward, G., Parsons, A., Biesecker, D. A., Hill, S., & Odstrcil, D. (2011). Wang-sheeley-arge-enlil cone model transitions to operations. *Space Weather*, *9*. doi: doi:10.1029/2011SW000663

Riley, P., Linker, J. A., & Miki, Z. (2001). An empirically-driven global mhd model of the solar corona and inner heliosphere. *Journal of Geophysical Research: Space Physics*, *106*(A8), 15889-15901. Retrieved from https://agupubs.onlinelibrary.wiley.com/doi/abs/10.1029/2000JA000121 doi:

10.1029/2000JA000121
Rollett, T., Möstl, C., Isavnin, A., Davies, J. A., Kubicka, M., Amerstorfer, U. V., & Harrison, R. A. (2016, June). ElEvoHI: A Novel CME Prediction Tool for Heliospheric Imaging Combining an Elliptical Front with Drag-based Model Fitting. *The Astrophysical Journal*, *824*, 131. doi: 10.3847/0004-637X/824/2/131
Rouillard, A. P., Sheeley, N. R., Jr., Cooper, T. J., Davies, J. A., Lavraud, B., Kilpua, E. K. J., ... Sauvaud, J.-A. (2011, June). The Solar Origin of Small Interplanetary Transients. *The Astrophysical Journal*, *734*, 7. doi: 10.1088/0004-637X/734/1/7
Sheeley, N. R., Walters, J. H., Wang, Y.-M., & Howard, R. A. (1999, November). Continuous tracking of coronal outflows: Two kinds of coronal mass ejections. *Journal of Geophysical Research*, *104*, 24739-24768. doi: 10.1029/1999JA900308
Sheeley, N. R., Jr., & Rouillard, A. P. (2010, May). Tracking Streamer Blobs into the Heliosphere. *The Astrophysical Journal*, *715*, 300-309. doi: 10.1088/0004-637X/715/1/300
Siscoe, G., & Odstrcil, D. (2008). Ways in which icme sheaths differ from magnetosheaths. *Journal of Geophysical Research: Space Physics*, *113*(A9). Retrieved from `https://agupubs.onlinelibrary.wiley.com/doi/abs/10.1029/2008JA013142` doi: 10.1029/2008JA013142
Stone, E. C., Frandsen, A. M., Mewaldt, R. A., Christian, E. R., Margolies, D., Ormes, J. F., & Snow, F. (1998, July). The Advanced Composition Explorer. *Space Science Reviews*, *86*, 1-22. doi: 10.1023/A:1005082526237
Tappin, S. J. (2017). Considerations for the use of stereo -hi data for astronomical studies. *The Astronomical Journal*, *153*(4), 164. Retrieved from `http://stacks.iop.org/1538-3881/153/i=4/a=164`
Webb, D. F., & Howard, T. A. (2012, Jun 29). Coronal mass ejections: Observations. *Living Reviews in Solar Physics*, *9*(1), 3. Retrieved from `https://doi.org/10.12942/lrsp-2012-3` doi: 10.12942/lrsp-2012-3
Xiong, M., Davies, J. A., Bisi, M. M., Owens, M. J., Fallows, R. A., & Dorrian, G. D. (2013, July). Effects of Thomson-Scattering Geometry on White-Light Imaging of an Interplanetary Shock: Synthetic Observations from Forward Magnetohydrodynamic Modelling. *Solar Physics*, *285*, 369-389. doi: 10.1007/s11207-012-0047-0